


ORIGINAL ARTICLE

Open Access



Comprehensive integrated analysis of MR and DCE-MR radiomics models for prognostic prediction in nasopharyngeal carcinoma

Hailin Li^{1,2†}, Weiyuan Huang^{3†}, Siwen Wang^{2,4}, Priya S. Balasubramanian⁵, Gang Wu⁶, Mengjie Fang^{1,2}, Xuebin Xie⁷, Jie Zhang⁸, Di Dong^{2,4*} , Jie Tian^{1,2,9,10*} and Feng Chen^{3*}

Abstract

Although prognostic prediction of nasopharyngeal carcinoma (NPC) remains a pivotal research area, the role of dynamic contrast-enhanced magnetic resonance (DCE-MR) has been less explored. This study aimed to investigate the role of DCE-MR in predicting progression-free survival (PFS) in patients with NPC using magnetic resonance (MR)- and DCE-MR-based radiomic models. A total of 434 patients with two MR scanning sequences were included. The MR- and DCE-MR-based radiomics models were developed based on 289 patients with only MR scanning sequences and 145 patients with four additional pharmacokinetic parameters (volume fraction of extravascular extracellular space (v_e), volume fraction of plasma space (v_p), volume transfer constant (K^{trans}), and reverse reflux rate constant (k_{ep}) of DCE-MR. A combined model integrating MR and DCE-MR was constructed. Utilizing methods such as correlation analysis, least absolute shrinkage and selection operator regression, and multivariate Cox proportional hazards regression, we built the radiomics models. Finally, we calculated the net reclassification index and C-index to evaluate and compare the prognostic performance of the radiomics models. Kaplan-Meier survival curve analysis was performed to investigate the model's ability to stratify risk in patients with NPC. The integration of MR and DCE-MR radiomic features significantly enhanced prognostic prediction performance compared to MR- and DCE-MR-based models, evidenced by a test set C-index of 0.808 vs 0.729 and 0.731, respectively. The combined radiomics model improved net reclassification by 22.9%–52.6% and could significantly stratify the risk levels of patients with NPC ($p=0.036$). Furthermore, the MR-based radiomic feature maps achieved similar results to the DCE-MR pharmacokinetic parameters in terms of reflecting the underlying angiogenesis information in NPC. Compared to conventional MR-based radiomics models, the combined radiomics model integrating MR and DCE-MR showed promising results in delivering more accurate prognostic predictions and provided more clinical benefits in quantifying and monitoring phenotypic changes associated with NPC prognosis.

Keywords Dynamic contrast-enhanced magnetic resonance imaging, Magnetic resonance imaging, Radiomics, Prognostic prediction

[†]Hailin Li and Weiyuan Huang should be considered joint first authors.

*Correspondence:

Di Dong

di.dong@ia.ac.cn

Jie Tian

jie.tian@ia.ac.cn

Feng Chen

fenger0802@163.com

Full list of author information is available at the end of the article

Introduction

As an endemic common malignancy, nasopharyngeal carcinoma (NPC) ranks first among head and neck malignant tumors with an incidence rate of 3.0 per 100,000 individuals in Southeast Asia [1]. Radiotherapy-based comprehensive treatment is regarded as the standard strategy for NPC. Although the prognosis has considerably improved with the popularization of intensity-modulated radiotherapy in the past decades, the 5-year survival rate remains approximately 60% in patients with locoregional advanced NPC [2]. The lack of responses to therapy, recurrence, and distant metastasis are the main causes of poor prognosis in NPC [3]. Pretreatment identification of adverse events is thus important to make individualized treatment decisions. In current clinical practice, tumor therapeutic response is only evaluated using RECIST (one-dimensional descriptors) or WHO (two-dimensional descriptors) criteria [4]. These criteria have significant potential in indicating therapeutic response but often fail to predict progression-free survival (PFS). The most commonly used benchmark for prognostic estimation of NPC is the tumor-node-metastasis (TNM) staging system. However, patients with similar treatment regimens or at the same stage can show large variations in clinical outcomes [5]. Thus, the present TNM staging system may not provide adequate prognostic information to comprehensively express the biological heterogeneity of NPC [6].

Magnetic resonance (MR) imaging plays an important role in NPC detection and staging. The excellent soft-contrast resolution of conventional MR can reveal the morphological features. Dynamic contrast-enhanced MR (DCE-MR) is an MR perfusion technique that consists of a series of rapid contrast-enhanced T1-weighted (CET1-w) acquisitions of serial MR images with high temporal resolution before and after the administration of clinically available contrast agents (i.e., gadolinium chelates). These contrast agents alter the signal intensity in the target tissues, which is proportional to their concentration. During analysis, signal intensities are converted into concentration curves, provided that a pre-contrast relaxation map is obtained and the relationship between signal intensity and concentration is known for the specific MR sequence used. With appropriate modeling, quantitative analysis allows for the inference of blood flow, blood volume, and vascular permeability, in addition to the morphological tumor characteristics used in clinical practice. The pharmacokinetic parameters of DCE-MR, such as volume fraction of extravascular extracellular space (v_e), volume fraction of plasma space (v_p), volume transfer constant (K^{trans}), and reverse reflux rate constant (k_{ep}), can potentially reflect angiogenesis and tumor aggressiveness [7]. Until now, many studies have utilized

DCE-MR to predict therapeutic response or prognosis in patients with NPC [8–10]. However, the concentration of the contrast agent in the vessel and the variability of arterial input function (AIF) have been considered the main reasons for the low dependability of DCE-MR [11–13].

Radiomics is a popular medical image analysis technique that involves image processing, feature engineering, and deep learning algorithms, which can extract features related to lesion shape, statistics, and texture and construct a mathematical model associated with clinical events [14–17]. In recent years, radiomics has significantly assisted clinicians in the early diagnosis, determination of treatment plans, and prognostic assessment of NPC [18–22]. Due to its fast speed, accurate calculation, and noninvasiveness, radiomics presents immense prospects for development. However, some unresolved issues, such as interpretability, are becoming serious obstacles. In most deep learning models, class activation mapping (CAM)-based methods [23, 24] can be used to generate visual explanation maps. However, for feature engineering-based radiomics models, the algorithm for generating radiomics feature maps still needs to be improved to present noteworthy regions inside the tumor. In previous radiomics studies, most of the predefined radiomic features tended to be calculated based on the global region of interest (ROI), while the visual representation of these features requires individual calculations from each local image patch and then overlaying the feature values of all patches onto the ROI [25]. Therefore, the image patch size may significantly affect the visual representation of radiomic features. The statistical calculation of radiomic features tends to be more accurate when a larger local image patch is selected; however, the resolution of the visualized image may be reduced accordingly. There is a compromise between accurate feature extraction and precise information localization, which restricts the patch size and step size settings.

Radiomics can help evaluate tumor heterogeneity and the microenvironment, and thus lead to the identification of novel predictors of prognosis [26, 27]. Radiomic analysis based on multiparametric MR has been successfully performed to predict individual PFS in patients with advanced NPC [28, 29]. Moreover, the radiomic features derived from MR images are useful for predicting the treatment response to chemoradiotherapy [30] and induction chemotherapy [31, 32] in patients with NPC. However, most previous studies have focused on conventional MR sequences. Recent studies have revealed that DCE-MR-based radiomics are more efficient than conventional MR sequences in predicting prognosis and evaluating treatment responses in malignant gliomas [33], breast cancer [34], and rectal cancer [35]. In addition, the prognostic predictive performance of MR-based

radiomics models has been reported to outperform traditional clinical models in previous radiomics studies [36–38]. In this study, we developed a radiomics model by combining MR and DCE-MR imaging features to predict PFS and assessed its incremental value in MR- and DCE-MR-based radiomics models. To test our hypothesis that MR-based radiomics features contain prognostic information related to the underlying angiogenesis and pharmacokinetic information, we further visualized MR-based radiomics feature maps on DCE-MR images.

Methods

This study was approved by the Institutional Review Board of Hainan General Hospital, which waived the requirement for written informed consent. The overall workflow includes patient enrollment, segmentation for

MR and DCE-MR images, radiomics feature extraction, radiomics model construction and assessment, as shown by the flowchart in Fig. 1. The open source PyRadiomics platform (version 3.0.1) was used in this study, which adheres to the image biomarker standardization initiative protocol.

Study population

This study enrolled patients with NPC from December 2014 to January 2021, and the inclusion and exclusion criteria can be found in [Supplementary Methods 1](#). As shown in Fig. 2, we first divided the patients into two cohorts based on whether they had corresponding DCE-MR images: the cohort with only MR images ($n=289$) was allocated to an MR training set and an MR test set at a ratio of 7:3. Another cohort with both MR

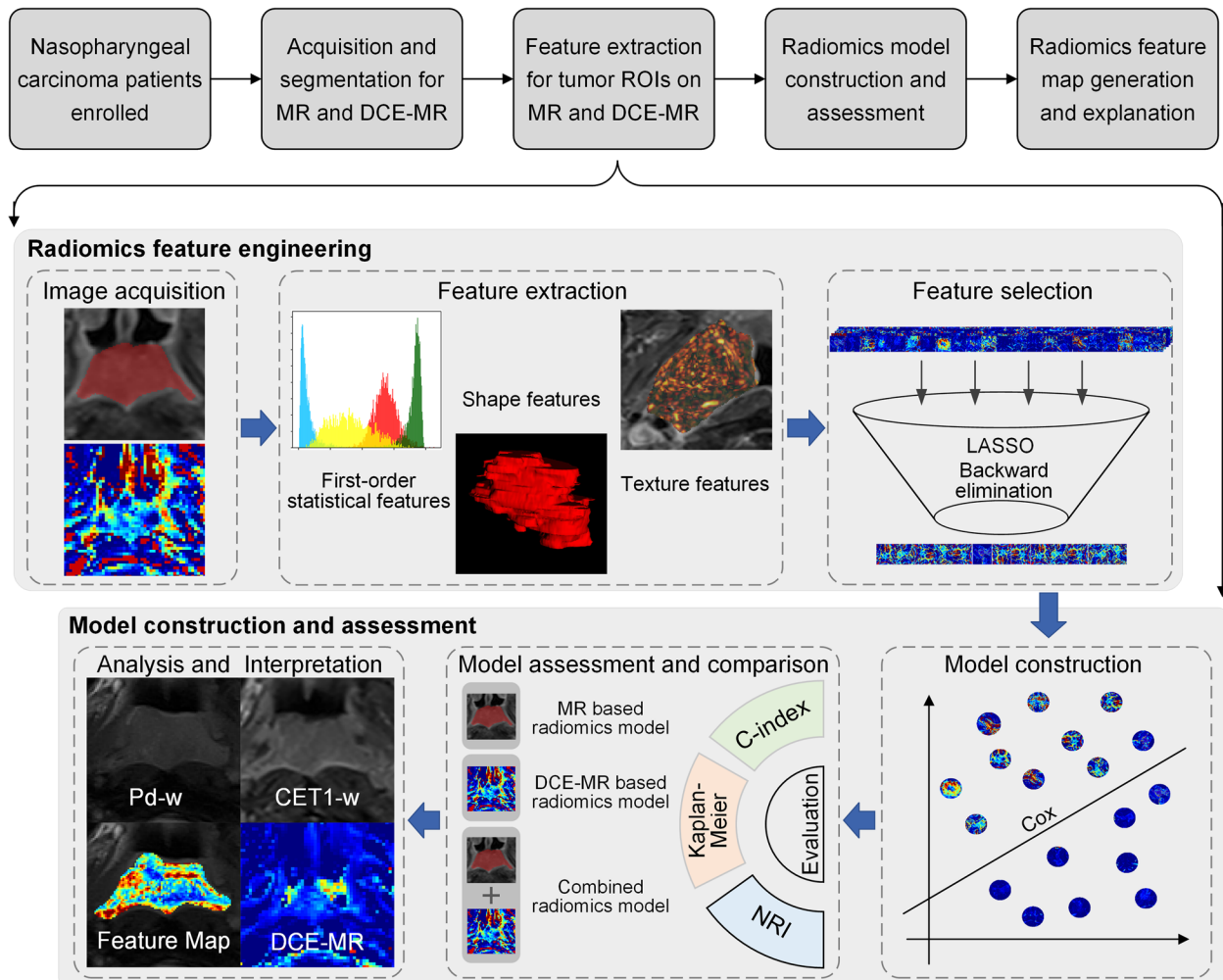


Fig. 1 Study layout. The MR based and DCE-MR based prognostic prediction models were constructed after image acquisition, feature extraction, and feature selection. The models were then assessed by C-index, Kaplan-Meier survival curve analysis, and NRI. Finally, four DCE-MR parameters and the radiomics feature map of MR based model were shown and analyzed

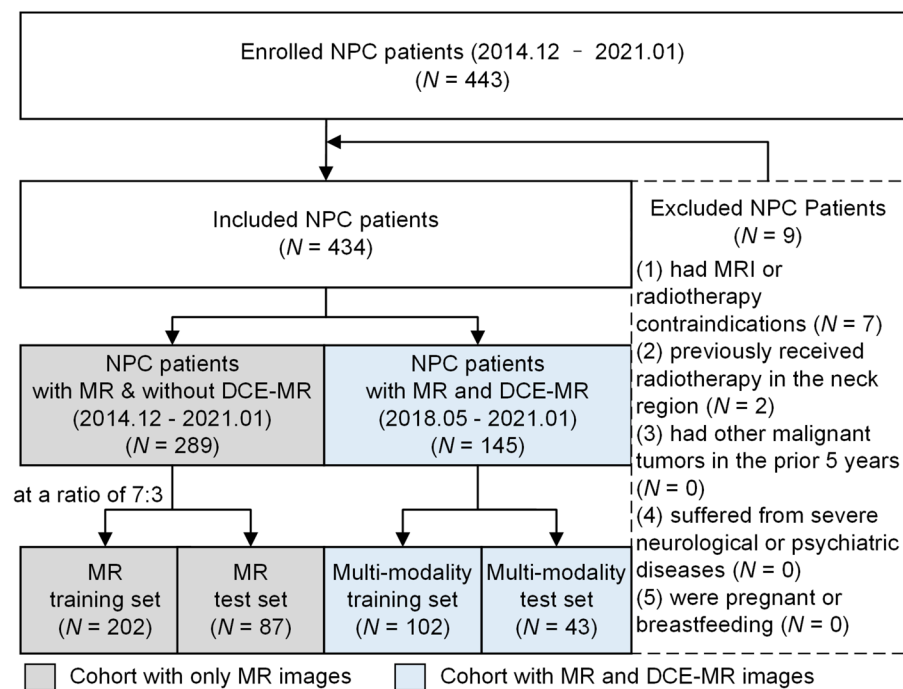


Fig. 2 Patient recruitment flowchart. A total of 434 patients were included in this study. The patients were then divided into two cohorts based on the presence or absence of DCE-MR images. The MR cohort with only MR images was randomly divided into an MR training set and test set at a ratio of 7:3. In addition, the multi-modality cohort with both MR and DCE-MR images was randomly allocated to a multi-modality training set and test set at a ratio of 7:3 as well. The MR cohort shown in the gray box and the multi-modality cohort in blue box constituted the whole dataset of this study

and DCE-MR images ($n = 145$) was allocated to a multi-modality training set and a multi-modality test set. An MR-based model was built on the MR training set and evaluated on the MR test set, and a DCE-MR-based model was built on the multi-modality training set and evaluated on the multi-modality test set. Because the multi-modality training and test sets contained not only DCE-MR images but also MR images, a combined model integrating the MR-based model and DCE-MR features was constructed and evaluated on these two sets.

Acquisition and segmentation for MR and DCE-MR

MR examinations were conducted using a 3.0 T MR system (Siemens Skyra, Erlangen, Germany) with a 20-channel head/neck coil. The detailed protocol can be found in [Supplementary Methods 2](#). The pharmacokinetic parameters (v_e , v_p , K^{trans} , and k_{ep}) of DCE-MR were estimated using the extended Tofts' linear model, with the intracranial internal carotid artery serving as the AIF. The three-dimensional ROIs of the primary lesions were manually delineated on proton density-weighted (PD-w) images, CET1-w images, and DCE-MR images slice-by-slice using ITK-SNAP (version 3.6.0, <http://www.itksnap.org>). The segmented ROIs were created by a junior radiologist (G.D. with 3-year experience) and further checked by a

senior radiologist (W.H. with 12-year experience), both of whom had no access to patients' clinical information.

Clinical endpoint and follow-up

Patients were assessed by MR examination every 3 months for the first 24 months, and then every 6 months. The endpoint of our study was PFS, which was defined as the time from the initial treatment to the first recurrence of the disease, death caused by NPC, or the latest follow-up visit, whichever occurred first. Disease progression was identified using pathological biopsy and/or imaging methods.

Image pre-processing and radiomics feature extraction

Based on the open-source PyRadiomics platform (version 3.0.1), we extracted three types of radiomics features for MR and DCE-MR images, including shape, first-order statistics, and texture features [39]. The shape features were only calculated on the original images (i.e., tumor ROIs). The texture features and first-order statistical features were also extracted from the derived images using filters. Because the MR signal is relative, with substantial differences between scanners and vendors, we normalized the image before the matrix-based texture feature calculation to reduce the confounding effect. Here, we

performed gray-value discretization using the window width of the five MR intensity values. The details of radiomics feature engineering can be found in [Supplementary Methods 3](#).

Construction and evaluation of MR based radiomics models

To identify a subset of features associated with PFS, we employed the least absolute shrinkage and selection operator (LASSO) method for radiomics feature selection on the MR training set using the ‘glmnet’ package in the R language. The selection of the λ parameter was performed based on tenfold cross-validation and the minimum error criterion. We then conducted backward feature elimination based on the p values in multivariate regression analysis. Finally, a multivariate Cox proportional hazards (CPH) regression model was used to build the radiomics model by fitting the aforementioned radiomic features. To address the issue of multicollinearity, we employed a variance inflation factor (VIF) function (‘car’ package in R language) to assess the presence of multicollinearity among all the feature considered in this study. Specifically, a VIF exceeding 5 was considered an indicator of multicollinearity. In this study, three MR-based radiomics models were constructed for PD-w images, CET1-w images, and their combinations (multi-sequence MR images). The model with the best prognostic prediction performance was selected for further comparison.

C-index was calculated to assess the prognostic performance of each model. In addition, Kaplan-Meier survival analysis was performed to investigate the ability of each model in risk stratification of patients with NPC, and a log-rank test was conducted to determine the statistical differences between the two risk groups.

Construction and evaluation of DCE-MR based radiomics models

In the multi-modality training set, five DCE-MR-based radiomics models were constructed using images of four DCE-MR parameters (v_e , v_p , K^{tran} , and k_{ep}) and their combination (multi-parameter DCE-MR-based model), following the same procedure as the MR-based radiomics models. In the construction of the multiparameter DCE-MR-based model, given the substantial interrelation among the numerous features in our original dataset, we initially employed Pearson correlation analysis to eliminate redundant features. Following this, consistent with the construction of MR-based models, we sequentially implemented LASSO regression and backward feature elimination for additional feature dimensionality reduction. Finally, the CPH regression was used to construct a survival analysis model. In Pearson correlation analysis,

we quantified the degree of similarity between pairwise features. Features that displayed a correlation coefficient exceeding 0.8 were deemed to have significant similarity. In these instances, one feature was arbitrarily excluded, thereby mitigating the covariance between features to a certain degree. DCE-MR-based radiomics models were evaluated using the same methods as the MR-based radiomics models in multimodality training and test sets.

Combined model based on MR and DCE-MR

To explore whether the DCE-MR radiomic features could improve the performance of the MR-based radiomics model, a combined model was constructed in a multimodality training set by integrating the DCE-MR radiomic features and an optimal MR-based radiomics model. Pearson’s correlation analysis was first performed to eliminate redundant DCE-MR radiomic features. To ensure that the DCE-MR-based model captured tumor information divergent from the MR-based model, features highly correlated (Pearson correlation analysis) with the MR-based radiomics model were eliminated. This refinement ensures an enhanced performance upon the fusion of both models. Finally, we incorporated the remaining DCE-MR radiomics features and MR-based radiomics model predictions and adopted LASSO regression and backward feature elimination to determine the PFS-related feature subset. Similarly, a multivariate CPH regression model was used to construct a combined model.

We calculated the C-index and conducted Kaplan-Meier survival curve analysis to evaluate the prognostic performance and risk stratification ability of the combined model in the DCE-MR test set. Additionally, the net reclassification index (NRI) was calculated to quantify the relative improvement of the combined model in prognostic prediction compared with the MR- and DCE-MR-based radiomics models.

MR based radiomics feature map

To extract features of the tumor ROIs more accurately, as well as to maintain a high resolution of the feature map, a sliding window algorithm with a larger window width (patch size) and a smaller step size was applied to calculate the radiomic features of image patches pixel by pixel. A larger window width (patch size) improves the accuracy of feature computation. However, a smaller step size (1 in this study) allows us to generate the final feature map with a higher image resolution. In this study, the length of the shortest edge of the outer rectangles of the tumor ROIs was 21. Consequently, the window size should be smaller than 21 to ensure that radiomic features are extracted from the inside area of the tumor. In addition, to obtain a relatively

large window width such that the extracted information could be more accurate, the window width was set to 21. It is worth highlighting that there is a compromise between too small a window size, which leads to inaccurate feature calculation, and too large a window size, which leads to excessive aggregation of information. Owing to the limitations of the tumor ROI size in this study, the optimal window size in practice needs to be investigated in more detail in future studies. Feature extraction was performed at the image patch level, and the feature values were concatenated according to the patch coordinates to form a feature matrix. We then overlaid the feature matrix onto the ROI of the MR images of PD-w/CET1-w to generate an MR-based

radiomics feature map. A more detailed generation process for the MR-based radiomics feature map is provided in [Supplementary Methods 4](#).

Results

Patient characteristics and clinical outcomes

A total of 443 consecutive patients newly diagnosed with NPC were enrolled, and 434 patients were included after verifying the exclusion criteria. The mean age was 49.13 ± 11.56 years. The median PFS was 27 months (range, 3–75 months). During follow-up, 70 patients showed disease progression. The patient characteristics in the MR and multimodality cohorts are summarized in [Table 1](#).

Table 1 Patient characteristics in MR and multi-modality cohorts

Characteristic	MR cohort		Multi-modality cohort	
	Training set (n = 202)	Test set (n = 87)	Training set (n = 102)	Test set (n = 43)
Sex				
Male	144 (71.3%)	65 (74.7%)	75 (73.5%)	29 (67.4%)
Female	58 (28.7%)	22 (25.3%)	27 (26.5%)	14 (32.6%)
Age				
Median (IQR)	48 (41–56)	49 (40–57)	49 (42–57)	51 (40–57)
≤ 40	50 (24.8%)	23 (26.4%)	19 (18.6%)	12 (27.9%)
40–50	67 (33.2%)	48 (55.2%)	63 (61.8%)	25 (58.1%)
> 50	85 (42%)	16 (18.4%)	20 (19.6%)	6 (14.0%)
T stage				
T1	7 (3.5%)	1 (1.2%)	3 (2.9%)	0 (0.0%)
T2	54 (26.7%)	32 (36.8%)	29 (28.4%)	6 (14.0%)
T3	84 (41.6%)	25 (28.7%)	48 (47.1%)	20 (46.5%)
T4	57 (28.2%)	29 (33.3%)	22 (21.6%)	17 (39.5%)
N stage				
N0	12 (5.9%)	6 (6.9%)	8 (7.8%)	1 (2.3%)
N1	49 (24.3%)	23 (26.4%)	28 (27.5%)	8 (18.6%)
N2	106 (52.5%)	47 (54.0%)	48 (47.1%)	19 (44.2%)
N3	35 (17.3%)	11 (12.7%)	18 (17.6%)	15 (34.9%)
M stage				
M0	199 (98.5%)	84 (96.6%)	100 (98.0%)	42 (97.7%)
M1	3 (1.5%)	3 (3.4%)	2 (2.0%)	1 (2.3%)
Overall stage				
I	2 (1.0%)	0 (0.0%)	0 (0.0%)	0 (0.0%)
II	18 (8.9%)	14 (16.1%)	11 (10.8%)	1 (2.3%)
III	93 (46.0%)	32 (36.8%)	57 (55.9%)	19 (44.2%)
IV	86 (42.6%)	37 (42.5%)	34 (33.3%)	23 (53.5%)
V	3 (1.5%)	4 (4.6%)	0 (0.0%)	0 (0.0%)
Follow-up time (mo)				
Median (IQR)	49 (23–61)	55 (34–63)	11 (7–17)	10 (6–19)

Independent-sample *t*-test was applied for continuous variables, and χ^2 test was applied for categorical variables. No significant differences were found between the MR and multi-modality cohorts in terms of sex, age, T stage, and N stage ($p = 0.315$ – 0.987). The M stage, overall stage, and follow-up time differed significantly between the two cohorts ($p = 2.96 \times 10^{-4}$, 0.015 , and 2.20×10^{-16} , respectively). IQR interquartile range

Construction and evaluation of MR based radiomics models

After data cleaning (deleting features with missing or repetitive values), 1681 and 1678 radiomic features were calculated based on the PD-w and CET1-w sequences, respectively. Two and four features were selected for the PD-w and CET1-w sequences, respectively, using LASSO-Cox regression. In addition, from the combination of features of the PD-w and CET1-w sequences, four radiomic features were screened out with significant multivariate regression coefficients ($p < 0.05$), including wavelet-LHL_glszm_LAHGLE and lbp_firstorder_Variance from the PD-w sequence, as well as wavelet-HHH_glszm_LAHGLE and squareroot_firstorder_RMAD from the CET1-w sequence. Finally, the PD-w-, CET1-w-, and multi-sequence MR-based radiomics models were constructed by fitting the selected features using multivariate CPH regression.

For the PD-w- and CET1-w-based radiomics models, the C-indices were 0.657 (95%CI: 0.549–0.765) and 0.664 (95% CI: 0.540–0.789) on the MR test set and 0.687 (95%CI: 0.582–0.791) and 0.626 (95%CI: 0.482–0.770) on the multi-modality test set, respectively. The multi-sequence MR-based radiomics model demonstrated the best prognostic prediction performance among the MR-based models, with a C-index of 0.729 (95%CI: 0.611–0.847) on the MR test set and 0.702 (95%CI: 0.547–0.857)

on the multi-modality test set. On the MR training and test sets, all three MR-based models performed well in the risk stratification of NPC, with statistical significance (log-rank test, $p < 0.05$). The multi-sequence MR based radiomics model achieved superior risk stratification ability among the three MR-based models. The Kaplan-Meier survival curves of the multi-sequence MR-based radiomics model are shown in Fig. 3. We used the median output values of the radiomics model in the training set as a cutoff to stratify patients into high- and low-risk groups.

Construction and evaluation of DCE-MR based radiomics models

We extracted 1392, 1395, 1391, and 1394 radiomic features from the images of the four pharmacokinetic parameters (v_e , v_p , K^{trans} , and k_{ep}). Similar to the feature selection and model construction processes of the PD-w- and CET1-w-based radiomics models, five, four, four, and six features were selected for v_e , v_p , K^{trans} , and k_{ep} based models, respectively. Four DCE-MR parameter-based models were constructed. To construct the multiparameter DCE-MR-based radiomics model, three features extracted from K^{trans} , v_e , and v_p were determined using Pearson correlation analysis and LASSO regression.

Five DCE-MR-based models were evaluated in the multi-modality test set, with a C-index of 0.654 (95%CI:

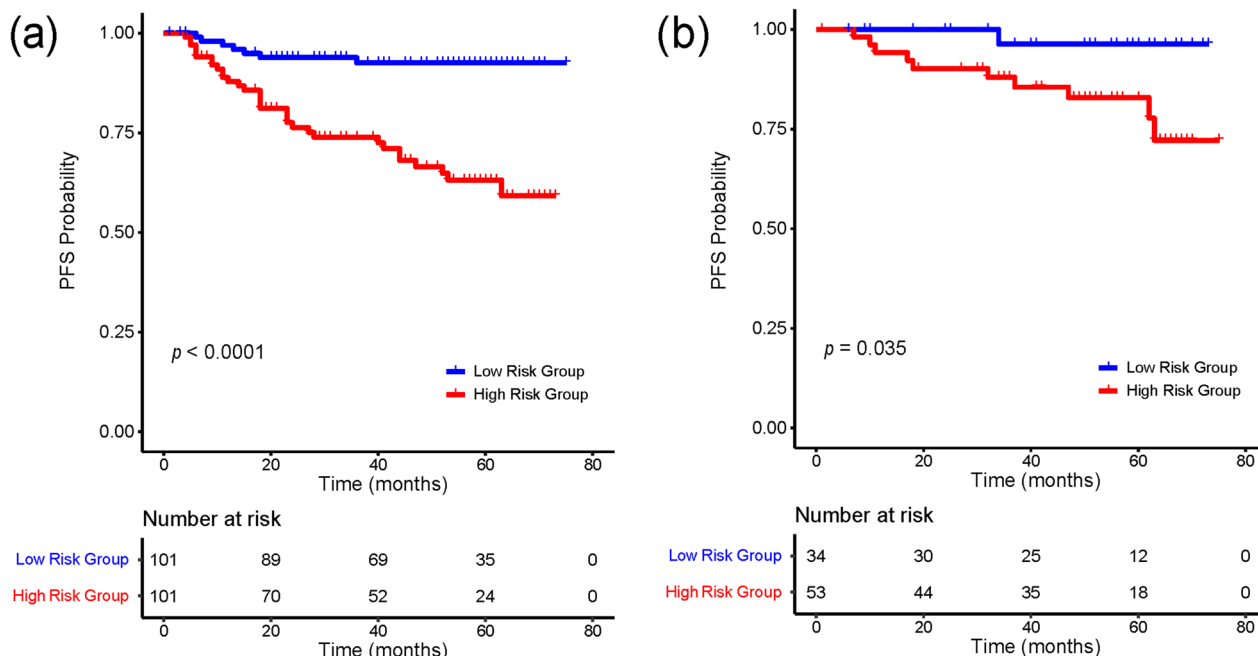


Fig. 3 Kaplan-Meier survival curve analysis of multi-sequence MR based radiomics model on MR cohort. Kaplan-Meier survival curves of multi-sequence MR based radiomics model on (a) MR training set and (b) MR test set. A p value < 0.05 was used to determine whether the difference was statistically significant between the low- and high-risk groups

0.493–0.815) for K^{trans} based model, 0.606 (95%CI: 0.378–0.834) for v_e based model, 0.587 (95%CI: 0.337–0.836) for v_p based model, 0.644 (95%CI: 0.458–0.830) for k_{ep} based model, and 0.731 (95%CI: 0.595–0.867) for the multi-parameter DCE-MR based model. Of the five models compared, the multi-parameter DCE-MR-based radiomics model achieved the highest C-index but still failed to significantly risk stratify NPC in the Kaplan-Meier survival curve analysis ($p=0.08$).

Construction and evaluation of combined radiomics model

We constructed a combined model by integrating the radiomic features of DCE-MRI and a multi-sequence MR-based radiomics model. After Pearson correlation analysis and LASSO regression, five features were selected: two texture features extracted from K^{trans} (maximal correlation coefficient and gray level non-uniformity normalized, abbreviated as MCC and GLNN), two texture features extracted from k_{ep} (complexity and large dependence high gray level emphasis, abbreviated as complexity and LDHGLE), and the prediction of the MR-based radiomics model. The detailed feature selection flow and LASSO-CV regression process are shown in [Supplementary Methods 3.5](#) and [3.6](#), respectively. By calculating the VIF, it was observed that all features had a VIF value below 5. The range of VIF values for the combined model and other models can be found in [Supplementary Methods 3.7](#). This finding demonstrates that the constructed radiomics regression model is stable and is not significantly affected by high multicollinearity among the features. The C-index of the combined radiomics model achieved 0.812 (95%CI: 0.620–0.989) on the multi-modality training set, and 0.808 (95%CI: 0.691–0.924) on the multi-modality test set. As shown in [Table 2](#), the combined radiomics model showed a statistically significant improvement in prognostic performance compared with all DCE-MRI- and MR-based models ($p<0.05$). Kaplan-Meier survival analysis ([Fig. 4c](#) and [d](#)) demonstrated that the combined radiomics model could significantly stratify the risk of NPC in the multi-modality training set ($p=0.028$) and multi-modality test set ($p=0.036$). To verify the robustness of our combined model across different age groups, sexes, T stages, and N stages, we performed subgroup analyses of these clinical parameters. The outcomes highlight the consistent performance of the combined model across these subgroups, with C-index values ranging from 0.779 to 0.810; no significant differences were observed between the different subgroups. Finally, we quantified the improvement of the combined radiomics model in prognostic prediction by computing the NRI, where the NRI achieved 0.526 (combined model vs multi-sequence MR-based model, 95% CI: 0.265–0.706) and 0.229 (combined model

Table 2 Performance of radiomics models on multi-modality test set

Model		C-index (95%CI)	p
MR based	PD-w	0.687 (0.582–0.791)	0.022
	CET1-w	0.626 (0.482–0.770)	0.032
	Multi-sequence MR	0.702 (0.547–0.857)	0.030
DCE-MR based	K^{trans}	0.654 (0.493–0.815)	0.002
	k_{ep}	0.644 (0.458–0.830)	0.013
	v_e	0.606 (0.378–0.834)	0.030
	v_p	0.587 (0.337–0.836)	0.027
	Multi-parameter DCE-MR	0.731 (0.595–0.867)	0.043
MR and DCE-MR	Combined	0.808 (0.691–0.924)	-

CI confidence interval, $p<0.05$, significant differences in C-indices between the combined model and MR/DCE-MR-based models

vs multi-parameter DCE-MR-based model, 95%CI: 0.134–0.579).

MR based radiomics feature map

As shown in [Fig. 5](#), a 41-year-old male patient with stage IV NPC (case 1) was confirmed to have metastasis at 3 months, and a 57-year-old male patient with stage IV NPC (case 2) did not experience any disease progression after treatment at 21 months. The tumor in case 1 showed a more obvious enhancement on CET1-w images and was more heterogeneous on PD-w images than that in case 2. DCE maps showed a similar tendency, with a poor prognosis case having higher perfusion and more heterogeneity in the tumor area. These characteristics were visualized to some extent using MR-based radiomics feature maps, particularly first-order feature maps (i.e., feature maps of `lbp_firstorder_Variance` in the PD-w sequence and `squareroot_firstorder_RMAD` in the CET1-w sequence). MR-based radiomics feature maps have the potential to be novel tools for visualizing tumor perfusion and heterogeneity. However, MR-based radiomics feature maps cannot reflect all the angiogenesis information of DCE-MR within tumors, which may also explain why DCE-MR features could help improve the performance of MR-based radiomics models in prognostic prediction.

Discussion

The combined radiomics model established in this study outperformed the MR based radiomics models as well as DCE-MR based radiomics models in prognosis prediction. This is primarily because angiogenesis information within tumors in DCE-MR complements MR-based radiomic features. In conventional MR-based radiomics, the models generated from the combination of PD-w and CET1-w images demonstrated

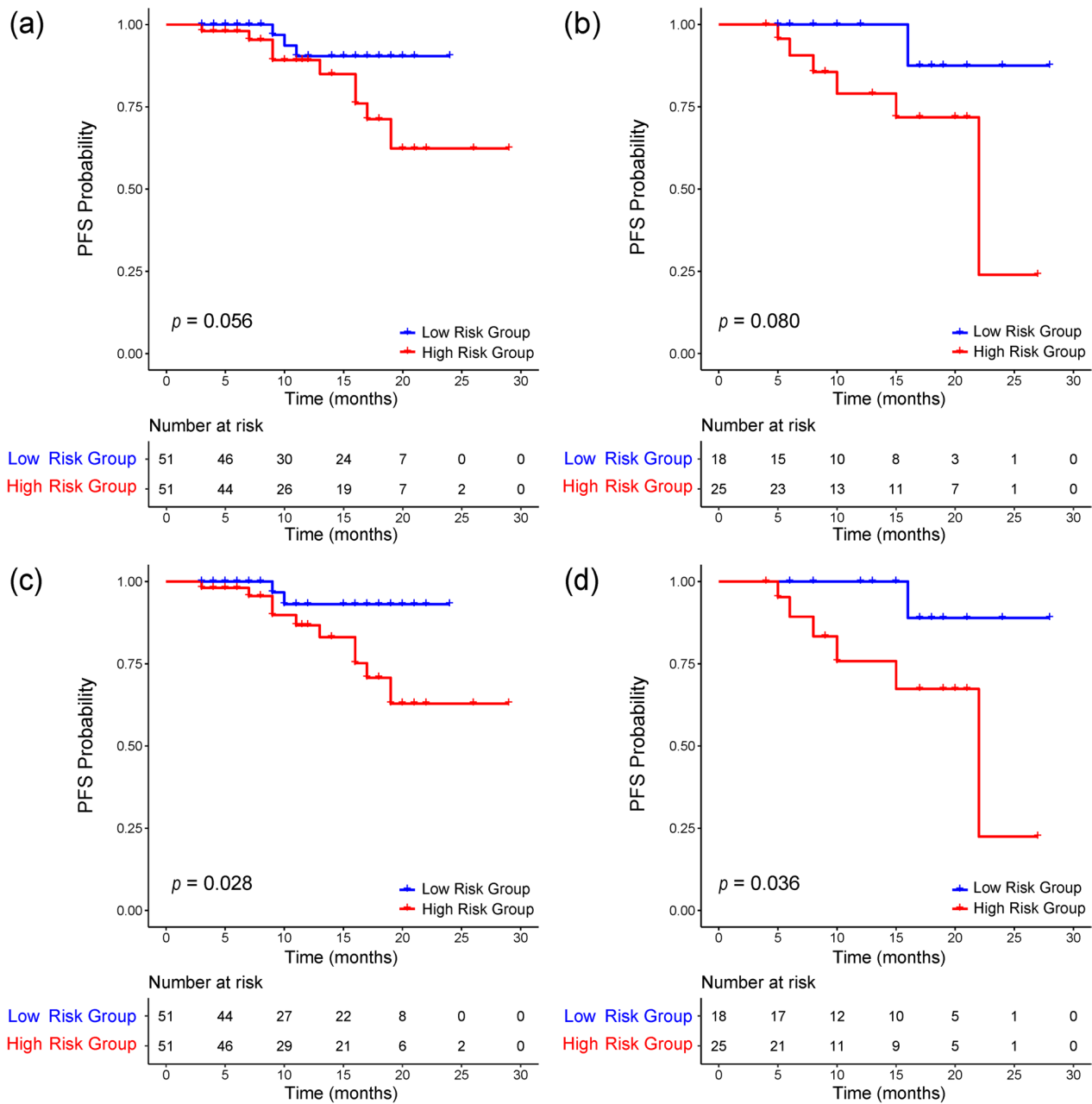


Fig. 4 Kaplan-Meier survival curve analysis of DCE-MR based radiomics model and the combined radiomics model on multi-modality cohort. Kaplan-Meier survival curves of multi-parameter DCE-MR based radiomics model on (a) multi-modality training set and (b) multi-modality test set; and the combined radiomics model on (c) multi-modality training set and (d) multi-modality test set. A p value < 0.05 was used to determine whether the difference was statistically significant between the low- and high-risk groups

better prognostic performance than the model from either PD-w or CET1-w alone, and all MR-based radiomics models could significantly stratify the risk levels of patients with NPC. In addition, in DCE-MR-based radiomics models, the joint analysis of multiple parameters enhanced the efficiency compared to any single parameter model but was still unable to achieve

significant risk stratification in patients with NPC. Furthermore, a high-resolution radiomics feature map was constructed to visualize and interpret the MR-based radiomic features, indicating that the MR-based radiomic features contained strong prognostic information, which might be interpreted using the underlying pharmacokinetic information quantitated by DCE-MR.

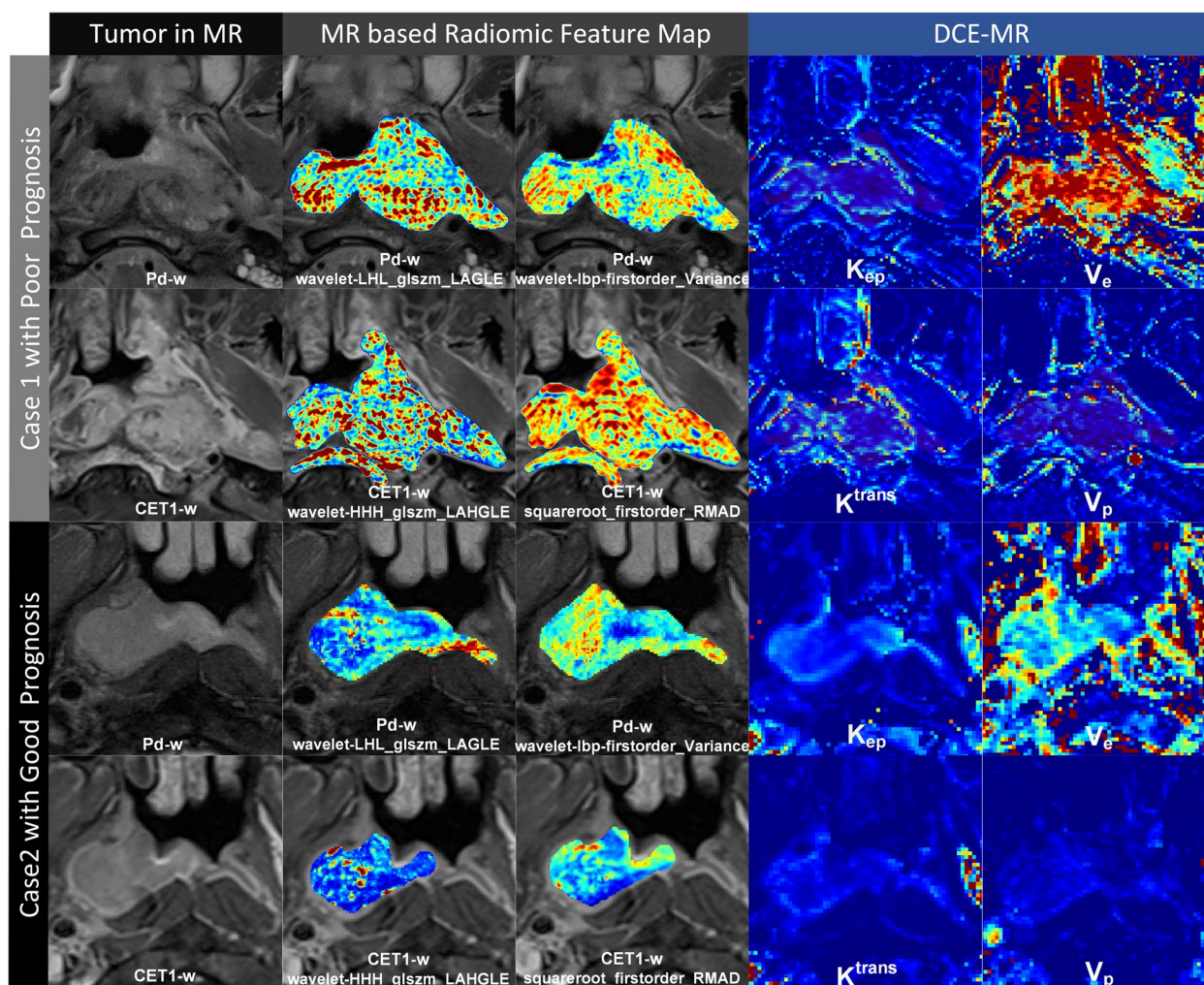


Fig. 5 Typical examples of poor prognosis and good prognosis. Each case provides 10 subgraphs, including 2 MR images, 4 radiomics feature maps and 4 DCE-MR parameter images. The name of each subgraph is marked below itself

Radiomic feature maps have the potential to visualize NPC prognosis to some extent.

Compared to traditional methods, radiomics provides a new train of thought for the potential associations between tumor angiogenesis and biological behaviors from a powerful and noninvasive perspective. Similar conclusions were reported in our previous study on advanced NPCs [29]. Only CET1-w and PD-w images were used to construct our radiomics models. Both the CET1-w and PD-w single-sequence models showed reliable capability in evaluating PFS, with the PD-w sequence model performing better. Their combination yielded significantly improved efficiency by integrating the morphological and functional features that affect the biological behavior of tumors. These results were similar to the naked-eye experience of radiologists in clinical practice. Unlike other tumors, the T staging of NPC mainly depends on the accurate tumor boundary information

provided by the PD-w rather than the CET1-w sequence. However, CET1-w images can capture flow and heterogeneity information using a contrast agent, which helps solve the problem in which the signal of the tumor invading the nasopharynx muscle on PD-w images looks similar to that of inflammatory edema.

DCE-MR, as a non-invasive imaging modality, shows potential in reflecting blood volume, blood flow, and vascular permeability [40]. In Malamas et al.'s [41] study, significant reductions in tumor blood flow, vascularity permeability, and plasma volume fraction were observed on DCE-MR in colon tumors. Our previous study also indicated significant correlations of DCE-MR pharmacokinetic parameters with EGFR and Ki-67 expression levels in NPC patients [7]. Thus, DCE-MR can detect tumor angiogenesis and heterogeneity by quantifying pharmacokinetic parameters, so as to realize non-invasive treatment monitoring and predict prognosis [8, 10,

42]. Our results revealed that the MR based radiomics model demonstrated better performance in risk stratification in patients with NPC than the DCE-MR based radiomics model. This may be because fast dynamic enhancement sequences achieve multiphase repeated scanning within a short time. Notably, our combined model did not show an obvious advantage, as illustrated by the Kaplan-Meier survival curve analysis, which may be due to the small size of the test set. However, these findings require further validation.

An MR-based radiomics model was constructed using two first-order statistical and two textural features. The two texture features were both large-area high-gray-level emphasis (LAHGLE) but were estimated on the PD-w and CET1-w sequences, respectively. LAHGLE computes the proportion of the joint distribution of larger zones with higher grey-level values within the tumor, reflecting tumor heterogeneity. Both first-order statistical features (variance and robust mean absolute deviation) reflected the uniformity of gray values in the tumors, suggesting that a more homogeneous tumor on PD-w or CET1-w images may indicate a better prognosis. The MR-based radiomics model and four DCE-MR radiomic features (extracted from K^{trans} and k_{ep} images). For K^{trans} , MCC measures the texture complexity and GLNN quantifies the similarity of pixel values. For k_{ep} , complexity focuses on rapid changes in pixel values, and LDHGLE computes the distribution of large dependence with higher grey-level values [39].

In our study, we found that the MR-based radiomics feature map showed promising consistency with the DCE parameter maps in terms of the NPC tumor boundary and heterogeneity. Radiomic features related to NPC prognosis were also identified to be associated with tumor heterogeneity in MR images [43]. However, the interpretability of radiomics is slightly poor, in addition to its quantitative ability. Compared with artificially assessed radiological measurements, there is a vacancy in the visual interpretation of the selected radiomic features, which motivated our attempts to form a reasonable interpretative tool for clinical practice. This challenge has been well recognized, and some researchers have made efforts to find correlations between radiomic features and known biological markers, such as HIF [44] or fibroblast growth factor receptor [45]. However, the biological data are often difficult to acquire because of complex protocols, while radiomic features containing more spatial and functional information are conveniently available. Akram et al.'s study [46] revealed that there was a substantial difference in MR-based radiomic features extracted from complete ROIs between recurrent and non-recurrent subregions in NPC treated with radiotherapy. Following a high success rate in risk stratification using MR-based

radiomic features, our results revealed that conventional MR-based radiomics might contain information with a similarly high impact on prognosis as angiogenesis information in accordance with DCE parameters. The above results suggest that MR-based radiomics feature maps can not only potentially visualize the heterogeneity and angiogenesis of the tumor from the ROI patches, but also allow tracing of the most revealing sub-regions in the analysis of a radiomics model.

Radiomics can be an effective method for monitoring phenotypic changes associated with prognosis in clinical settings. Our results revealed that radiomic features contained useful prognostic information in patients with NPC, and that the radiomics feature maps could visualize the heterogeneity and angiogenesis information of tumors, thereby improving the interpretation ability of radiomics. These results suggest that radiomics can decode the general phenotype associated with NPC prognosis. However, the conventional MR-based radiomics feature map showed similar but incomprehensive heterogeneity compared to the DCE parameter maps. A comparison between the MR-based radiomics feature map and the four pharmacokinetic parameters of DCE-MR images showed that not all the angiogenesis information on DCE-MR could be reflected by the radiomic features, which may explain why the integration of DCE-MR features and MR-based radiomics model prediction can significantly improve prognostic performance. Note that in the process of generating feature map, an essential observation is that the tumor ROI dimensions dictate the maximum window width during the feature map creation. Hence, an impending challenge lies in developing methods that assess the fidelity of model-used features, particularly at this maximum window width.

This study has several limitations. First, despite our efforts to include an exhaustive patient database, elevated censoring rates may have biased our findings. As a requirement for robustness, it is paramount to further validate our model against a dataset enriched with more extensive data. Second, the paucity of DCE-MR patients relative to the abundance of radiomic features necessitates meticulous feature selection to avoid overfitting. As the DCE-MR patient cohort expands in future work, there is the potential to incorporate more radiomic features. This would allow us to mine comprehensive prognostic prediction information, thereby enhancing the performance of our model. Third, the widespread use of DCE-MR came much later than that of conventional MR, resulting in a significant difference in follow-up between the MR and multi-modality cohorts. The drastically shorter follow-up of the DCE-MR cohort may harm the ability to build a convincing model to some extent. More DCE-MR-based radiomics studies with longer follow-up

periods should be conducted. Fourth, although the VIF analysis was performed on the final selected set of features to mitigate the impact of multicollinearity on the final model, the regression models constructed during the feature selection process were still susceptible to multicollinearity. In this study, we followed common practices observed in previous research; however, it is important to optimize this aspect in future studies. Finally, given that certain studies indicate that NRIs in the context of inadequately fitted risk functions can at times be misleading [47], we urge readers to approach conclusions regarding the NRIs in our study with due circumspection.

Conclusions

A combined radiomics model was identified by integrating DCE-MR and MR, which outperformed conventional MR-based radiomics models and can be used as an artificial intelligence tool for individualized prognostic assessment before treatment in patients with NPC.

Abbreviations

MR	Magnetic resonance
DCE-MR	Dynamic contrast-enhanced magnetic resonance
NRI	Net reclassification index
LASSO	Least absolute shrinkage and selection operator
NPC	Nasopharyngeal carcinoma
IQR	Interquartile range
CET1-w	Contrast-enhanced T1-weighted
PFS	Progression-free survival
TNM	Tumor-node-metastasis
v_e	Volume fraction of extravascular extracellular space
v_p	Volume fraction of plasma space
K^{trans}	Volume transfer constant
k_{ep}	Reverse reflux rate constant
AIF	Arterial input function
ROI	Region of interest
PD-w	Proton density-weighted
CPH	Cox proportional hazards
VIF	Variance inflation factor
LAHGLE	Large-area high-gray-level emphasis

Supplementary Information

The online version contains supplementary material available at <https://doi.org/10.1186/s42492-023-00149-0>.

Additional file 1.

Acknowledgements

The authors acknowledge instrumental and technical support from the Multimodal Biomedical Imaging Experimental Platform, Institute of Automation, Chinese Academy of Sciences. This study was supported by Hainan Province Clinical Medical Center.

Authors' contributions

HL contributed to conceptualization, investigation, methodology, software and writing-original draft; WH contributed to methodology, data curation, writing-original draft; SW contributed to methodology, writing-review and editing; PSB contributed to methodology, writing-review and editing; GW contributed to conceptualization, resources; MF contributed to methodology, investigation; XX contributed to validation, supervision; JZ contributed to conceptualization, resources, supervision; DD contributed to conceptualization,

funding acquisition, writing-review and editing; JT contributed to conceptualization, supervision, funding acquisition; FC contributed to data curation, funding acquisition. All the authors have read and approved the final manuscript.

Funding

This work was supported by the Natural Science Foundation of Hainan Province, No.821MS125; the National Key R&D Program of China, No. 2023YFC2415200; the Key R & D projects in Hainan Province, No. ZDYF-2021SHFZ239; the Natural Science Research Project "open competition mechanism" of Hainan Medical College, Nos. JBGS202113 and JBGS202107; Strategic Priority Research Program of the Chinese Academy of Sciences, No. XDB 38040200; National Natural Science Foundation of China, Nos. 82372053, 82302296, 81871346, 81971602, 82022036, 91959130, 81971776, 81771924, 62027901, 81930053; Beijing Natural Science Foundation, No. L182061 and Z20J00105; Chinese Academy of Sciences, Nos. GJJSTD20170004 and QYZDJ-SSW-JSC005; and Youth Innovation Promotion Association CAS, No. 2017175.

Availability of data and materials

The datasets used and analyzed in the current study are available from the corresponding author upon reasonable request.

Declarations

Competing interests

The authors have no relevant conflicts of interest to disclose.

Author details

¹Beijing Advanced Innovation Center for Big Data-Based Precision Medicine, School of Medicine and Engineering, Beihang University, Beijing 100191, China. ²CAS Key Laboratory of Molecular Imaging, Institute of Automation, Chinese Academy of Sciences, Beijing 100190, China. ³Department of Radiology, Hainan General Hospital (Hainan Affiliated Hospital of Hainan Medical University), Haikou, Hainan 570311, China. ⁴School of Artificial Intelligence, University of Chinese Academy of Sciences, Beijing 100049, China. ⁵Department of Psychiatry, Weill Cornell Medicine, New York, NY 10065, USA. ⁶Department of Radiotherapy, Hainan General Hospital (Hainan Affiliated Hospital of Hainan Medical University), Haikou, Hainan 570311, China. ⁷Department of Radiology, Kiang Wu Hospital, Santo António, Macao 999078, China. ⁸Department of Radiology, Zhuhai People's Hospital (Zhuhai Hospital Affiliated With Jinan University), Zhuhai, Guangdong 519000, China. ⁹Engineering Research Center of Molecular and Neuro Imaging of Ministry of Education, School of Life Science and Technology, Xidian University, Xi'an, Shaanxi 710126, China. ¹⁰Zhuhai Precision Medical Center, Zhuhai People's Hospital, Zhuhai, Guangdong 519000, China.

Received: 29 June 2023 Accepted: 27 October 2023

Published online: 01 December 2023

References

- Chen YP, Chan ATC, Le QT, Blanchard P, Sun Y, Ma J (2019) Nasopharyngeal carcinoma. *Lancet* 394(10192):64–80. [https://doi.org/10.1016/S0140-6736\(19\)30956-0](https://doi.org/10.1016/S0140-6736(19)30956-0)
- Emanuel O, Liu J, Scharfingher VH, Nei WL, Chan YY, Tsang CM et al (2021) SSTR2 in nasopharyngeal carcinoma: relationship with latent EBV infection and potential as a therapeutic target. *Cancers* 13(19):4944. <https://doi.org/10.3390/cancers13194944>
- Lee AWM, Ng WT, Chan JYW, Corry J, Mäkitie A, Mendenhall WM et al (2019) Management of locally recurrent nasopharyngeal carcinoma. *Cancer Treat Rev* 79:101890. <https://doi.org/10.1016/j.ctrv.2019.101890>
- Cao XJ, Song J, Xu J, Gong GZ, Yang XH, Su Y et al (2021) Tumor blood flow is a predictor of radiotherapy response in patients with nasopharyngeal carcinoma. *Front Oncol* 11:567954. <https://doi.org/10.3389/fonc.2021.567954>

5. Wang HY, Sun BY, Zhu ZH, Chang ET, To KF, Hwang JSJ et al (2011) Eight-signature classifier for prediction of nasopharyngeal carcinoma survival. *J Clin Oncol* 29(34):4516–4525. <https://doi.org/10.1200/JCO.2010.33.7741>
6. Shen LJ, Li W, Wang SY, Xie GF, Zeng Q, Chen C et al (2016) Image-based multilevel subdivision of M1 category in TNM staging system for metastatic nasopharyngeal carcinoma. *Radiology* 280(3):805–814. <https://doi.org/10.1148/radiol.2016151344>
7. Huang WY, Zhang QH, Wu G, Chen PP, Li J, Gillen KM et al (2021) DCE-MRI quantitative transport mapping for noninvasively detecting hypoxia inducible factor-1 α , epidermal growth factor receptor overexpression, and Ki-67 in nasopharyngeal carcinoma patients. *Radiother Oncol* 164:146–154. <https://doi.org/10.1016/j.radonc.2021.09.016>
8. Mui AWL, Lee AWM, Lee VHF, Ng WT, Vardhanabhuti V, Man SSS et al (2021) Prognostic and therapeutic evaluation of nasopharyngeal carcinoma by dynamic contrast-enhanced (DCE), diffusion-weighted (DW) magnetic resonance imaging (MRI) and magnetic resonance spectroscopy (MRS). *Magn Reson Imaging* 83:50–56. <https://doi.org/10.1016/j.mri.2021.07.003>
9. Zheng DC, Chen YB, Liu XY, Chen Y, Xu LY, Ren W et al (2015) Early response to chemoradiotherapy for nasopharyngeal carcinoma treatment: value of dynamic contrast-enhanced 3.0 T MRI. *J Magn Reson Imaging* 41(6):1528–1540. <https://doi.org/10.1002/jmri.24723>
10. Qin YH, Yu XP, Hou J, Hu Y, Li FP, Wen L et al (2019) Prognostic value of the pretreatment primary lesion quantitative dynamic contrast-enhanced magnetic resonance imaging for nasopharyngeal carcinoma. *Acad Radiol* 26(11):1473–1482. <https://doi.org/10.1016/j.acra.2019.01.021>
11. You SH, Choi SH, Kim TM, Park CK, Park SH, Won JK et al (2018) Differentiation of high grade from low-grade astrocytoma: improvement in diagnostic accuracy and reliability of pharmacokinetic parameters from DCE MR imaging by using arterial input functions obtained from DSC MR imaging. *Radiology* 286(3):981–991. <https://doi.org/10.1148/radiol.2017.70764>
12. Othman AE, Falkner F, Kessler DE, Martirosian P, Weiss J, Kruck S et al (2016) Comparison of different population-averaged arterial-input-functions in dynamic contrast-enhanced MRI of the prostate: effects on pharmacokinetic parameters and their diagnostic performance. *Magn Reson Imaging* 34(4):496–501. <https://doi.org/10.1016/j.mri.2015.12.009>
13. Azahaf M, Haberley M, Betrouni N, Ernst O, Behal H, Duhamel A et al (2016) Impact of arterial input function selection on the accuracy of dynamic contrast-enhanced MRI quantitative analysis for the diagnosis of clinically significant prostate cancer. *J Magn Reson Imaging* 43(3):737–749. <https://doi.org/10.1002/jmri.25034>
14. Kumar V, Gu YH, Basu S, Berglund A, Eschrich SA, Schabath MB et al (2012) Radiomics: the process and the challenges. *Magn Reson Imaging* 30(9):1234–1248. <https://doi.org/10.1016/j.mri.2012.06.010>
15. Lambin P, Leijenaar RTH, Deist TM, Peerlings J, de Jong EEC, van Timmeren J et al (2017) Radiomics: the bridge between medical imaging and personalized medicine. *Nat Rev Clin Oncol* 14(12):749–762. <https://doi.org/10.1038/nrclinonc.2017.141>
16. Gillies RJ, Kinahan PE, Hricak H (2016) Radiomics: images are more than pictures, they are data. *Radiology* 278(2):563–577. <https://doi.org/10.1148/radiol.2015151169>
17. Cattell R, Ying J, Lei L, Ding J, Chen SL, Sosa MS et al (2022) Preoperative prediction of lymph node metastasis using deep learning-based features. *Vis Comput Ind Biomed Art* 5(1):8. <https://doi.org/10.1186/s42492-022-00104-5>
18. Zhang L, Dong D, Li HL, Tian J, Ouyang FS, Mo XK, et al (2019) Development and validation of a magnetic resonance imaging-based model for the prediction of distant metastasis before initial treatment of nasopharyngeal carcinoma: a retrospective cohort study. *eBioMedicine* 40:327–335. <https://doi.org/10.1016/j.ebiom.2019.01.013>
19. Zhong LZ, Fang XL, Dong D, Peng H, Fang MJ, Huang CL et al (2020) A deep learning MR-based radiomic nomogram may predict survival for nasopharyngeal carcinoma patients with stage T3N1M0. *Radiother Oncol* 151:1–9. <https://doi.org/10.1016/j.radonc.2020.06.050>
20. Zhong LZ, Dong D, Fang XL, Zhang F, Zhang N, Zhang LW et al (2021) A deep learning-based radiomic nomogram for prognosis and treatment decision in advanced nasopharyngeal carcinoma: a multicentre study. *eBioMedicine* 70:103522. <https://doi.org/10.1016/j.ebiom.2021.103522>
21. Dong D, Zhang F, Zhong LZ, Fang MJ, Huang CL, Yao JJ et al (2019) Development and validation of a novel MR imaging predictor of response to induction chemotherapy in locoregionally advanced nasopharyngeal cancer: a randomized controlled trial substudy (NCT01245959). *BMC Med* 17(1):190. <https://doi.org/10.1186/s12916-019-1422-6>
22. Wang ZP, Fang MJ, Zhang J, Tang LQ, Zhong LZ, Li HL et al (2023) Radiomics and deep learning in nasopharyngeal carcinoma: a review. *IEEE Rev Biomed Eng* (in press). <https://doi.org/10.1109/RBME.2023.3269776>
23. Zhou BL, Khosla A, Lapedriza A, Oliva A, Torralba A (2016) Learning deep features for discriminative localization. In: Proceedings of the IEEE conference on computer vision and pattern recognition, IEEE, Las Vegas, 27–30 June 2016. <https://doi.org/10.1109/CVPR.2016.319>
24. Selvaraju RR, Cogswell M, Das A, Vedantam R, Parikh D, Batra D (2017) Grad-CAM: visual explanations from deep networks via gradient-based localization. In: Proceedings of the IEEE international conference on computer vision, IEEE, Venice, 22–29 October 2017. <https://doi.org/10.1109/ICCV.2017.74>
25. Fehr D, Veeraghavan H, Wibmer A, Gondo T, Matsumoto K, Vargas HA et al (2015) Automatic classification of prostate cancer Gleason scores from multiparametric magnetic resonance images. *Proc Natl Acad Sci USA* 112(46):E6265–E6273. <https://doi.org/10.1073/pnas.1505935112>
26. Zhao X, Liang YJ, Zhang X, Wen DX, Fan W, Tang LQ et al (2022) Deep learning signatures reveal multiscale intratumor heterogeneity associated with biological functions and survival in recurrent nasopharyngeal carcinoma. *Eur J Nucl Med Mol Imaging* 49(8):2972–2982. <https://doi.org/10.1007/s00259-022-05793-x>
27. Li HL, Wang SW, Liu B, Fang MJ, Cao RN, He BX et al (2023) A multi-view co-training network for semi-supervised medical image-based prognostic prediction. *Neural Networks* 164:455–463. <https://doi.org/10.1016/j.neunet.2023.04.030>
28. Yang KX, Tian JF, Zhang B, Li M, Xie WJ, Zou YT et al (2019) A multidimensional nomogram combining overall stage, dose volume histogram parameters and radiomics to predict progression-free survival in patients with locoregionally advanced nasopharyngeal carcinoma. *Oral Oncol* 98:85–91. <https://doi.org/10.1016/j.oraloncology.2019.09.022>
29. Zhang B, Tian J, Dong D, Gu DS, Dong YH, Zhang L et al (2017) Radiomics features of multiparametric MRI as novel prognostic factors in advanced nasopharyngeal carcinoma. *Clin Cancer Res* 23(15):4259–4269. <https://doi.org/10.1158/1078-0432.CCR-16-2910>
30. Liu J, Mao Y, Li ZJ, Zhang DK, Zhang ZC, Hao SN et al (2016) Use of texture analysis based on contrast-enhanced MRI to predict treatment response to chemoradiotherapy in nasopharyngeal carcinoma. *J Magn Reson Imaging* 44(2):445–455. <https://doi.org/10.1002/jmri.25156>
31. Wang GY, He L, Yuan C, Huang YQ, Liu ZY, Liang CH (2018) Pretreatment MR imaging radiomics signatures for response prediction to induction chemotherapy in patients with nasopharyngeal carcinoma. *Eur J Radiol* 98:100–106. <https://doi.org/10.1016/j.ejrad.2017.11.007>
32. Zhao LN, Gong J, Xi YB, Xu M, Li C, Kang XW et al (2020) MRI-based radiomics nomogram may predict the response to induction chemotherapy and survival in locally advanced nasopharyngeal carcinoma. *Eur Radiol* 30(1):537–546. <https://doi.org/10.1007/s00330-019-06211-x>
33. Wang CH, Sun WZ, Kirkpatrick J, Chang Z, Yin FF (2018) Assessment of concurrent stereotactic radiosurgery and bevacizumab treatment of recurrent malignant gliomas using multi-modality MRI imaging and radiomics analysis. *J Radiosurg SBRT* 5(3):171–181
34. Montemezzi S, Benetti G, Bisighin MV, Camera L, Zerbato C, Caumo F et al (2021) 3T DCE-MRI radiomics improves predictive models of complete response to neoadjuvant chemotherapy in breast cancer. *Front Oncol* 11:630780. <https://doi.org/10.3389/fonc.2021.630780>
35. Palmisano A, Esposito A, Rancoita PMV, Di Chiara A, Passoni P, Slim N et al (2018) Could perfusion heterogeneity at dynamic contrast-enhanced MRI be used to predict rectal cancer sensitivity to chemoradiotherapy? *Clin Radiol* 73(10):911.e1–911.e7. <https://doi.org/10.1016/j.crad.2018.06.007>
36. Jiang HT, Piao YF, Ye ZM, Jiang CE, Jiang YM, Wang FZ (2022) Development and validation of a pre-treatment magnetic resonance imaging radiomics-based signature to predict progression-free survival in patients with locally advanced nasopharyngeal carcinoma. *SSRN* 4156709. <https://doi.org/10.2139/ssrn.4156709>
37. Shen HS, Wang Y, Liu DH, Lv RF, Huang YY, Peng C et al (2020) Predicting progression-free survival using MRI-based radiomics for patients with nonmetastatic nasopharyngeal carcinoma. *Front Oncol* 10:618. <https://doi.org/10.3389/fonc.2020.00618>

38. Kim MJ, Choi Y, Sung YE, Lee YS, Kim YS, Ahn KJ et al (2021) Early risk-assessment of patients with nasopharyngeal carcinoma: the added prognostic value of MR-based radiomics. *Transl Oncol* 14(10):101180. <https://doi.org/10.1016/j.tranon.2021.101180>
39. van Griethuysen JJM, Fedorov A, Parmar C, Hosny A, Aucoin N, Narayan V et al (2017) Computational radiomics system to decode the radiographic phenotype. *Cancer Res* 77(21):e104–e107. <https://doi.org/10.1158/0008-5472.CAN-17-0339>
40. Meyer HJ, Hamerla G, Leifels L, Höhn AK, Surov A (2019) Histogram analysis parameters derived from DCE-MRI in head and neck squamous cell cancer—Associations with microvessel density. *Eur J Radiol* 120:108669. <https://doi.org/10.1016/j.ejrad.2019.108669>
41. Malamas AS, Jin EL, Gujrati M, Lu ZR (2016) Dynamic contrast enhanced MRI assessing the antiangiogenic effect of silencing HIF-1 α with targeted multifunctional ECO/siRNA nanoparticles. *Mol Pharmaceutics* 13(7):2497–2506. <https://doi.org/10.1021/acs.molpharmaceut.6b00227>
42. Jansen JFA, Lu YG, Gupta G, Lee NY, Stambuk HE, Mazaheri Y et al (2016) Texture analysis on parametric maps derived from dynamic contrast-enhanced magnetic resonance imaging in head and neck cancer. *World J Radiol* 8(1):90–97. <https://doi.org/10.4329/wjrv.8.i1.90>
43. Cui CY, Wang SX, Zhou J, Dong AN, Xie F, Li HJ et al (2020) Machine learning analysis of image data based on detailed MR image reports for nasopharyngeal carcinoma prognosis. *Biomed Res Int* 2020:8068913. <https://doi.org/10.1155/2020/8068913>
44. Gkika E, Benndorf M, Oerther B, Mohammad F, Beitinger S, Adebahr S et al (2020) Immunohistochemistry and radiomic features for survival prediction in small cell lung cancer. *Front Oncol* 10:1161. <https://doi.org/10.3389/fonc.2020.01161>
45. Dong D, Fang MJ, Tang L, Shan XH, Gao JB, Giganti F, et al (2020) Deep learning radiomic nomogram can predict the number of lymph node metastasis in locally advanced gastric cancer: an international multi-center study. *Ann Oncol* 31(7):912–920. <https://doi.org/10.1016/j.annonc.2020.04.003>
46. Akram F, Koh PE, Wang FQ, Zhou SQ, Tan SH, Paknezhad M et al (2020) Exploring MRI based radiomics analysis of intratumoral spatial heterogeneity in locally advanced nasopharyngeal carcinoma treated with intensity modulated radiotherapy. *PLoS One* 15(10):e0240043. <https://doi.org/10.1371/journal.pone.0240043>
47. Pepe MS, Fan J, Feng ZD, Gerds T, Hilden J (2015) The net reclassification index (NRI): a misleading measure of prediction improvement even with independent test data sets. *Stat Biosci* 7(2):282–295. <https://doi.org/10.1007/s12561-014-9118-0>

Publisher's Note

Springer Nature remains neutral with regard to jurisdictional claims in published maps and institutional affiliations.

Submit your manuscript to a SpringerOpen[®] journal and benefit from:

- Convenient online submission
- Rigorous peer review
- Open access: articles freely available online
- High visibility within the field
- Retaining the copyright to your article

Submit your next manuscript at ► [springeropen.com](https://www.springeropen.com)
